Experiments in Fluids (2021) 62:18
https://doi.org/10.1007/s00348-020-03106-2

RESEARCH ARTICLE

The impact of upstream turbulence on a plane jet

Md Kamruzzaman[1] · Olav Rømcke[1] · R. Jason Hearst[1]

Received: 5 June 2020 / Revised: 14 November 2020 / Accepted: 23 November 2020
© The Author(s) 2021

Abstract

The influence of upstream turbulence on the flow produced by a plane jet is investigated experimentally with hot-wire anemometry and smoke flow visualisation. An innovative active grid, where each wing can be independently controlled, is used to change the upstream turbulence conditions. Three cases are investigated: a canonical reference case, a case with the same integral scale as the reference case but an order of magnitude increase in turbulence intensity, and a case with both an order of magnitude increase in turbulence intensity and an order of magnitude increase in integral scale compared to the reference case. It is demonstrated that the wake width increases with turbulence intensity, but decreases with integral scale for constant turbulence intensity. In addition, the positional variability of the wake width is highest with high turbulence intensity and a short integral scale. Along the jet centreline, the potential core region is shorter with elevated upstream turbulence intensity; this is reflected in both the mean velocity and the variance. The decay of the centreline mean velocity is also retarded by incoming turbulence. In all, increased incoming turbulence results in increased jet spreading, and a shorter integral scale further increases the spreading.

Graphic abstract

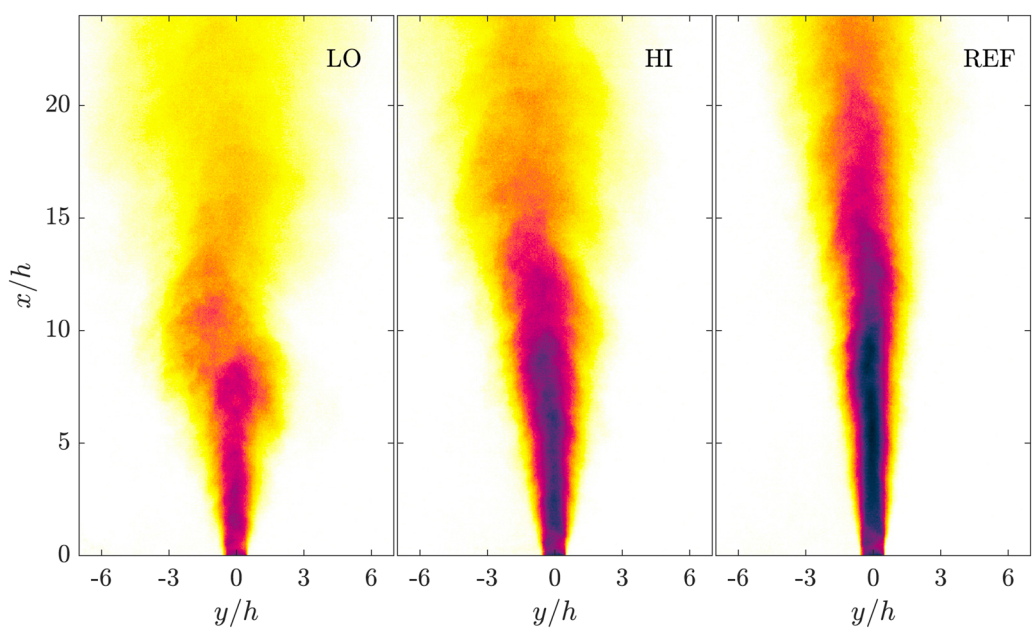

✉ R. Jason Hearst
jason.hearst@ntnu.no

[1] Department of Energy and Process Engineering, Norwegian University of Science and Technology, Kolbjørn Hejes vei 2, 7491 Trondheim, Norway

1 Introduction

The plane jet is a canonical flow of both historical and contemporary significance. It is a relatively simple flow with well understood initial and boundary conditions, allowing

Published online: 08 January 2021

for the development of analytical expressions for its evolution that can be validated against experiments, c.f., George (1989); Pope (2000); Cafiero and Vassilicos (2019). It is also a simplification of many practical flows of engineering interest, e.g., air curtains (Maurel et al. 2000), building ventilation (Törnström et al. 2001), flow control actuators (Gutmark and Grinstein 1999). The conceptual plane jet is a thin flow source emanating from an infinitely long nozzle resulting in a predominantly 2-dimensional flow. In simulations, this is typically implemented as a high aspect-ratio rectangular jet with periodic boundary conditions on the thin edges of the jet, e.g., Watanabe et al. (2019). In experiments, the plane jet is typically implemented as a high aspect-ratio rectangular jet, e.g., Deo et al. (2007a).

Experimentalists have spent a great deal of effort modifying the plane jet design with a goal of producing the best approximation of a top-hat velocity distribution at the jet exit with an approximately 2-dimensional flow field. Nathan et al. (2000) and Deo et al. (2007b) explored several different nozzle geometries. They found that the centreline decay and spreading rate are significantly influenced by the geometry, and ultimately recommended that a ratio of the nozzle exit radius (r) to the jet height should be $r/h \geq 1.8$ to produce a top-hat profile. Bashir and Uberoi (1975) looked at the effect of aspect-ratio of the nozzle with relatively large discretizations of 20, 40 and 140, concluding that the aspect-ratio 20 jet was not particularly 2-dimensional. Deo et al. (2007a) explored this topic in greater detail and recommended that a minimum aspect ratio of 30 is required for approximately 2D flow. Hitchman et al. (1990) and Deo et al. (2007c) placed sidewalls on the short edges of the jet and found that their presence improved the 2-dimensionality of the flow. Finally, Deo et al. (2008) studied the effect of varying the jet Reynolds number, $\mathrm{Re}_h = U_b h/\nu$ where U_b is the bulk velocity at the jet exit, h is the nozzle height and ν is the kinematic viscosity. They found that for $\mathrm{Re}_h < 10,000$ there were substantial Reynolds number effects despite the exit velocity profile being approximately a top-hat distribution. Summarizing these results, to produce an approximately 2-dimensional plane jet with a top-hat velocity profile at the nozzle exit one should: have a nozzle with $r/h \geq 1.8$, an aspect ratio of at least 30, use sidewalls, and $\mathrm{Re}_h \geq 10,000$.

After producing the idealised jet flow, several studies have focused on using passive techniques to modulate the jet development. For example, Rajagopalan and Antonia (1998) placed small cylinders in the exit plane of the plane jet and found that they reduced the growth rate and suppressed the turbulent fluctuations. Similar strategies have been employed for axisymmetric round jets (Parker et al. 2003; Sadeghi and Pollard 2012), corroborating that these methods result in reduced growth rate and suppressed turbulent motions.

Passive grids have also been used to modulate axisymmetric jets. Rajagopalan et al. (2013) placed passive meshes both slightly inside their nozzle and at the exit. They focused on two geometries of grids, one that completely covered the nozzle and one that only covered the potential core. The mesh that completely covered the nozzle yielded similar results to the control rings, decreasing the growth rate and turbulence intensity, while the mesh that only covered the potential core resulted in increased energy in the shear layers, enhancing the turbulence intensity and growth rate. Kumar et al. (2015) placed five different passive grids at the outlet of their nozzle. In general, the grids reduced the turbulence intensity and slowed the growth rate, in agreement with Rajagopalan et al. (2013). They also noted that they did not observe vortex roll-up in the shear layers for their cases with grids. Cafiero et al. (2015a) investigated the effect of placing a square fractal grid at the nozzle exit and measured up to a position approximately $10D$ downstream. They showed that this grid enhanced the turbulence intensity downstream, roughly behaving similar to the partial mesh of Rajagopalan et al. (2013) instead of the full meshes or the control rings. It is worth noting that subsequent multi-scale grid turbulence measurements have demonstrated that this enhanced turbulence resulting from the fractal geometry is in part a consequence of being close to the grid relative to the largest scale in the grid, and that more traditional results are recovered if measurements are performed farther downstream (Krogstad and Davidson 2011, 2012; Hearst and Lavoie 2014, 2016).

Some investigations have also focused on the impact of forced methods of modulating mixing layers and jets. For example, the seminal work of Oster and Wygnanski (1982) examined the sensitivity of shear mixing layer to surging/forcing. Generally, they found that the forcing results in an increase in spreading rate. Koochesfahani and Dimokaris (1989) investigated the effects of disturbance on the plane mixing layer by pitching an airfoil within it. They found that the growth rate of shear layers was dependent on the forcing frequency and generally low frequencies resulted in smaller wake widths. Aydemir et al. (2012) investigated the vortex ring formation in a forced round jet and found that the jet-breakup depends on both amplitude and frequency of the upstream forcing. Their forcing was applied acoustically with speakers, but their amplitude and frequency roughly correspond to the concepts of turbulence intensity and length scale in a broadband fully turbulent flow.

The significant body of research that exists on canonical jet flows has predominately been focused on reproducing these fundamental flows accurately, or on modulating the flow around the nozzle. There has been little focus on the impact of upstream turbulence on the flow beyond the jet exit, with the notable exception of Rajagopalan et al. (2013), who did do test cases with the grid placed slightly upstream

of the nozzle exit, but did not contract the flow after the grid and did not observe appreciably different results from placing the grid at the exit. Nonetheless, this is a question of significant practical interest. Consider for instance a ventilation duct exit that does not have a large contraction or flow conditioning section upstream of it. Is it realistic to model this flow as an idealised plane jet, which is the common practice? In the present study, we focus on modulating the flow immediately upstream of the nozzle and measuring what impact this has on the near-field jet spreading and the far-field centreline statistics. The upstream turbulence is generated with a novel active grid where each wing is controlled independently, similar to the work of Griffin et al. (2019). The active grid is used because it can produce high levels of turbulence and orders of magnitude changes in the length scales (Larssen and Devenport 2011; Hearst and Lavoie 2015).

2 Experimental setup

2.1 Facility and active grid

The planar jet facility is shown schematically in Fig. 1. A centrifugal blower pushes air through a diffuser with a series of screens before the flow is contracted. The contraction is 1.9 m long and has a contraction ratio of 49:1 (from 1.215 m × 1.215 m to 0.6 m × 0.05 m) following a fifth-order polynomial curve.

An active grid with 24 independently controlled wings is mounted in a straight duct that extends 130 mm downstream of the end of the contraction. The wings are arranged in a 12 × 2 layout as shown in Fig. 1b and c. Each wing is individually connected to a Moons' STM17S-3RE stepper motor. The wings have a size of 48 mm × 24.5 mm × 2 mm. The straight duct extends another 90 mm downstream of the active grid before the flow encounters a 2D nozzle. The nozzle was 3D printed with an inner wall radius of 40 mm following the guidelines provided by Deo et al. (2007b) for producing an approximately top-hat jet profile. This nozzle geometry resulted in a planar jet with exit height $h = 20$ mm, and an aspect ratio of 30; the latter was shown by Deo et al. (2007a) to be sufficient to produce approximately 2D flow. Plywood sidewalls were mounted on the two short sides of the planar jet in order to reduce spreading in this dimension, thus promoting 2-dimensionality (Deo et al. 2007b, c; Cafiero and Vassilicos 2019). The sidewalls extended 2.4 m = $120h$ downstream of the jet nozzle. The planar jet thus propagates in the streamwise x-direction and spreads in the lateral y-direction only. The advantage of this jet configuration is that the results are statistically 2-dimensional over a reasonably large downstream distance (Deo et al. 2007c).

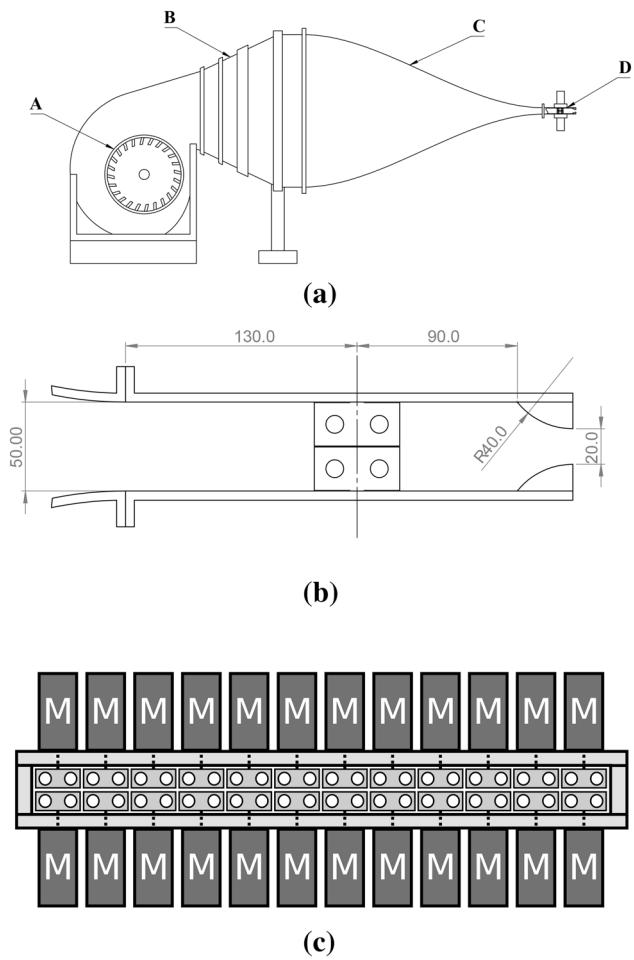

Fig. 1 Schematic of the experimental setup. The facility as a whole is shown in **a** where A is the centrifugal fan, B is the diffuser section with four screens, C is the 49:1 contraction, and D is the active grid and nozzle. In **b** a detailed view of the nozzle section housing the active grid is provided (units are in mm). A transverse schematic of the active grid is provided in **c**, showing the wings and the motors

2.2 Hot-wire measurements

The jet bulk velocity was kept fixed at $U_b = 8$ m/s for all cases, resulting in $\mathrm{Re}_h = U_b h/\nu \approx 10,000$. The velocity measurements were performed in the range $0 \le x/h \le 100$ along the centreline of the jet. For $1 \le x/h \le 10$, we also measured at 58 lateral positions by traversing the probe with an automated traverse. The measurements were carried-out under iso-thermal conditions with an ambient temperature of 20 ± 0.2°C. The probe itself was a Dantec 55P11 single-wire sensor, mounted with a Dantec probe holder and connected to a Dantec StreamLine Pro Constant Temperature Anemometer (CTA). The overheat ratio of the wire was 1.8. The temperature was also measured continuously for the entire duration of the hot-wire acquisition using an Omega T-type thermocouple with a resolution 0.1°C.

Hot-wire calibrations were carried-out using a standard Pitot-static tube placed beside the hot-wire probe at the jet's exit ($x/h \approx 0$) before and after each measurement case. The hot-wire was calibrated over the velocity range 0.2 m/s $\leq U_b \leq$ 15.6 m/s. The pre- and post-calibrations were interrogated for discrepancies, and if the velocity drift exceeded 0.5% then the experiment was repeated. No correction to the velocity was applied. A fifth-order polynomial curve was used for converting voltages to velocities. The obtained signals were low-pass filtered. For most of the measurements, the filter cutoff frequency was set at 10 kHz and the data were sampled at 30 kHz for $t_s = 180$ s, resulting in 72,000 jet exit turn-overs ($U_b t_s/h$) at each measurement station. The uncertainty on the mean velocity measurements is 0.5% which derives from the pressure transducer during calibration. The uncertainty on the velocity fluctuations, u' is $\pm$2.5%, estimated using the same procedure as Curvier (2012b).

2.3 Flow visualization

Flow visualization was used to qualitatively observe the spread of the jet, and optically confirm the hot-wire results. Instantaneous visualizations for each case are provided in Fig. 2. To visualize the jet, a Martin Magnum 2500 Hz smoke generator was placed at the inlet of the fan. LEDs illuminated the smoke jet at the nozzle exit, as a Photron FASTCAM Mini WX100 (4 mega-pixel sensor), with a 50 mm lens recorded the flow. The recording was captured at a frame rate of 125 Hz for 60 s. In between every flow visualization measurement, a short recording of the background, which was coloured black, was captured. The background measurements were subtracted in post-processing to improve the contrast of the visualization.

3 Initial conditions

The active grid was used to create three different sets of initial conditions upstream of the nozzle exit. For all three cases, the active grid was in position. For the reference case, REF, the active grid wings were set in their fully open position and thus acted more as a flow straightener upstream of the nozzle. For the LO and HI cases, the wings of the grid were operated in fully random sequences to produce roughly homogeneous turbulence (Hearst and Lavoie 2015). Each wing was fed a random velocity signal centred about Ω and varying by $\pm\omega$ (see Table 1); for both cases the ratio $\Omega/\omega = 2$ was kept constant. The selected cases were chosen because their rotational speed differed by an order of magnitude. Interestingly, changing the rotational speed of the wings resulted primarily in changes to the integral scale (L_{uu}) at the jet exit, while the turbulence intensity (u'_0/U_b) and Taylor microscale Reynolds number ($\mathrm{Re}_\lambda = \langle u'^2 \rangle^{1/2} \lambda/\nu$) remained approximately constant. This contrasts with typical observations for active grids in wind tunnel flows where both the turbulence intensity and integral scale are strongly affected by $\Omega \pm \omega$ (Larssen and Devenport 2011; Hearst and

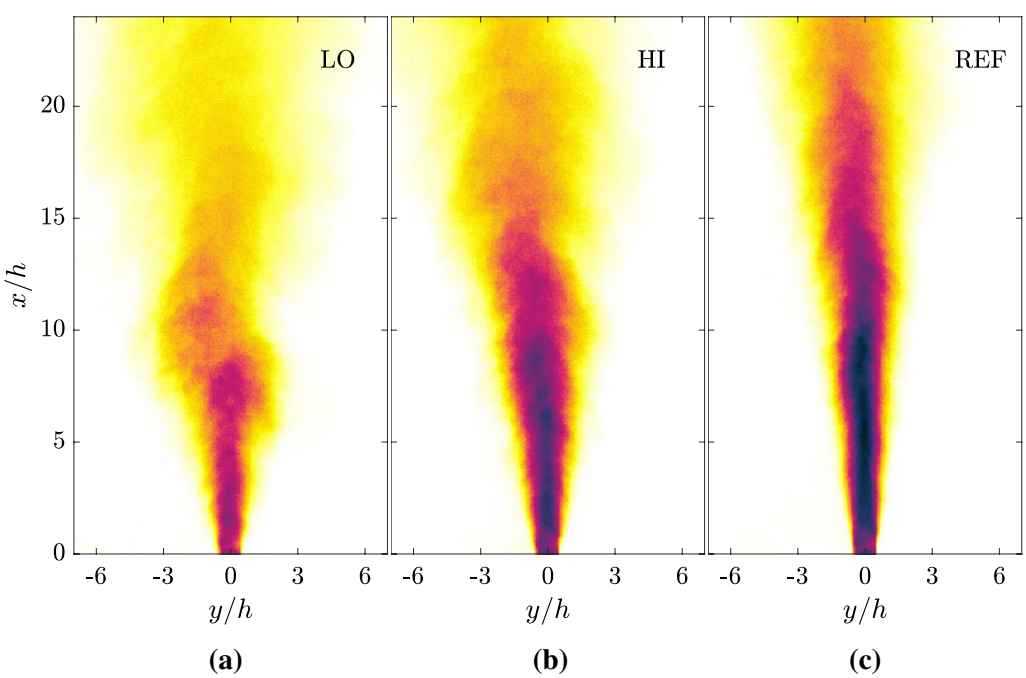

Fig. 2 Representative instantaneous flow visualizations for each case. Colours are arbitrary and roughly correspond to seeding density

Table 1 Turbulent statistics at the jet exit $(x/h, y/h) = (0, 0)$ for all cases

Cases	$\Omega \pm \omega$ [Hz]	u_0'/U_b [%]	Re_λ	L_{uu} [mm]	λ [mm]	η [mm]
REF	–	2.0	35	27	3.1	0.27
LO	9 ± 3	11.2	110	26	1.8	0.09
HI	0.75 ± 0.25	12.1	130	300	2.0	0.09

The mean velocity was kept constant at $U_b = 8$ m/s, $\mathrm{Re}_h \approx 10,000$ for all cases

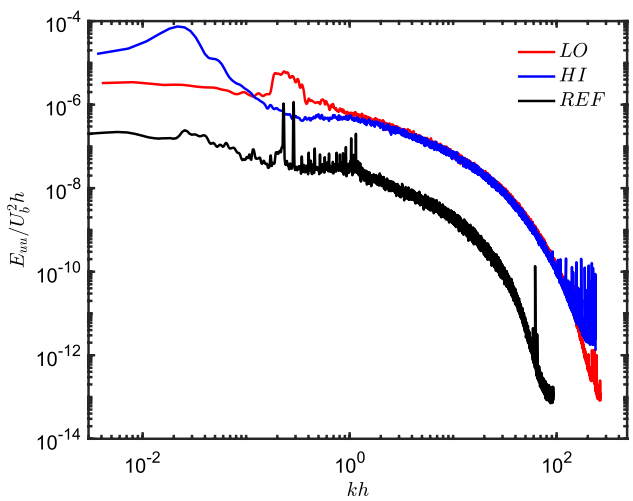

Fig. 3 One-dimensional energy spectra at the exit of the jet $(x/h = 0)$ normalised by large-scale parameters

Lavoie 2015). The difference in the present study is likely a result of the nozzle downstream of the grid. Nonetheless, this results in flows where the incoming turbulence intensity is approximately constant to within 1% of U_b and Re_λ changes by only 8%, while the integral scale changes by an order of magnitude. Turbulent statistics at the nozzle exit for the investigated cases are provided in Table 1. For reference, the spectra at the nozzle exit are provided in Fig. 3, demonstrating that they primarily differ at the large scales.

In the present study the integral scale was estimated from the integral of the autocorrelation to the first zero-crossing. The Kolmogorov microscale, identifying the approximate size of the smallest scales in the flow responsible for dissipation, is given by $\eta = \left(\nu^3/\langle\epsilon\rangle\right)^{1/4}$, where $\langle\epsilon\rangle$ is the mean dissipation rate of turbulent kinetic energy. The Taylor microscale (λ) is given by $\lambda = \left(\langle u'^2\rangle/\langle(\partial u/\partial x)^2\rangle\right)^{1/2}$, where Taylor's frozen flow hypothesis $\left(\overline{\left(\frac{\mathrm{d}}{\mathrm{d}x}\right)^2} = \frac{1}{U^2}\overline{\left(\frac{\mathrm{d}}{\mathrm{d}t}\right)^2}\right)$ is used for converting the temporal derivative acquired by the hot-wire into a spatial derivative along the streamwise direction.

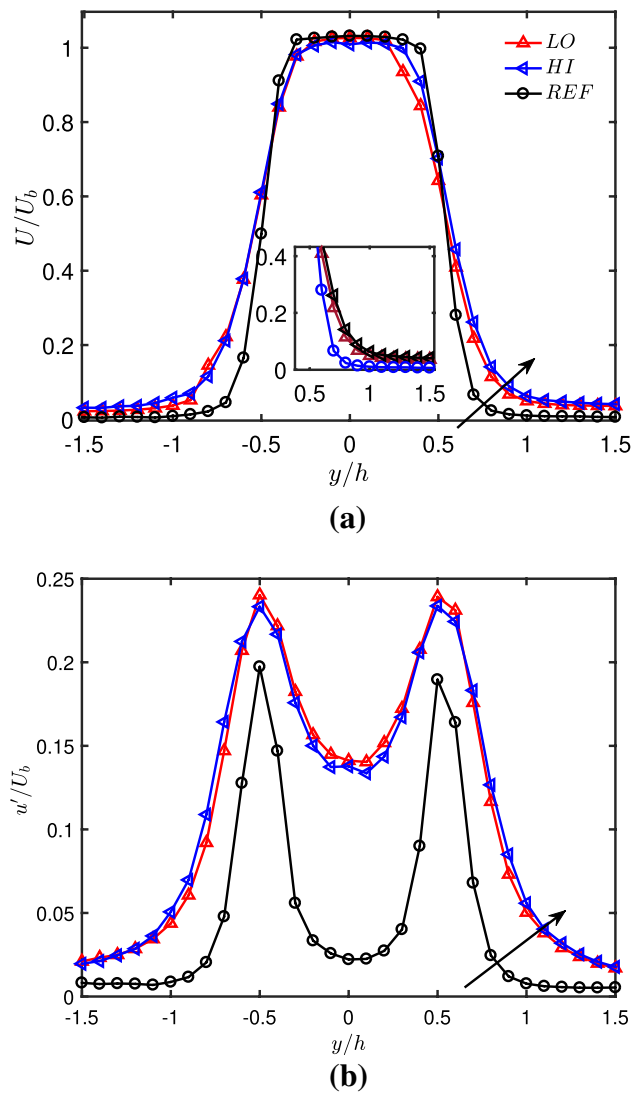

Fig. 4 Profiles of the normalised **a** mean velocity and **b** turbulence intensity measured $x/h = 1$ for all cases. The arrow indicates the direction of increasing incoming turbulence intensity

Figure 4 shows the mean velocity (U) and velocity fluctuation (u') profiles for the different cases at $x/h = 1$,

thus helping to characterise their difference. All cases produced an approximately top-hat mean exit velocity, with the REF case being the best approximation. The increase in turbulence intensity at the nozzle appears to cause the jet to spread earlier, as even at $x/h = 1$ the edges of the wake are farther from the centreline for both active grid cases compared to the reference case. Moreover, the jet is more rounded for the cases with higher incoming turbulence intensity. The velocity fluctuation profiles in Fig. 4b demonstrate that the turbulence intensity in the potential core of the jet is significantly elevated by the incoming turbulence generated by the active grid. Furthermore, the enhanced jet spreading, even at this position very close to the nozzle, is already evident.

4 The near-field of the jet

Lateral scans of the mean streamwise velocity at five locations in the near-field of the jet ($x/h \leq 10$) are shown for each case in Fig. 5. Focusing on the REF case (Fig. 5c), the jet exhibits the canonical behaviour whereby the magnitude of the velocity on the centreline decreases and the wake width grows as one moves downstream. This behaviour is also present for the incoming turbulence cases (Fig. 5a and b), however, we see a systematic evolution between the cases. For LO (Fig. 5a) with the smaller incoming integral scale, we see the fastest mean spreading of the wake width and the largest drop of the centreline mean velocity. As the integral scale becomes larger, the wake width becomes smaller. This is illustrated explicitly at $x/h = 7$ in Fig. 6. This result is further corroborated by the flow visualisation. The seeding used for the flow visualisation is effectively a scalar that tracks the instantaneous position of the jet. By taking an average of all acquired visualisation images, we gain an understanding of the mean position of the jet and its spreading. Figure 7 shows the average pixel intensity of all recorded instantaneous flow visualisation images for each case, with the hot-wire measurements overlayed.

A more explicit measure of the wake spreading is given by the evolution of the wake half-width ($\delta_{1/2}$) and the momentum thickness $\left(\theta = \int_{-\infty}^{+\infty} \frac{U}{U_b}\left(1 - \frac{U}{U_b}\right)\mathrm{d}y\right)$, both provided in Fig. 8. Here, we estimate $\delta_{1/2}$ in the same way as Oster and Wygnanski (1982); that is, $\delta_{1/2} = y_{0.95} - y_{0.10}$, where $y_{0.95}$ and $y_{0.10}$ correspond to the location at which $U(y_{0.95}) = U_{\min} + 0.95(U_{\max} - U_{\min})$ and $U(y_{0.10}) = U_{\min} + 0.1(U_{\max} - U_{\min})$, respectively. Figure 8 demonstrates that both $\delta_{1/2}$ and θ increase with streamwise position for all cases, and that the wake spreading is fastest for LO, followed by HI, with REF having the slowest spreading. Comparing LO and REF, which have similar integral

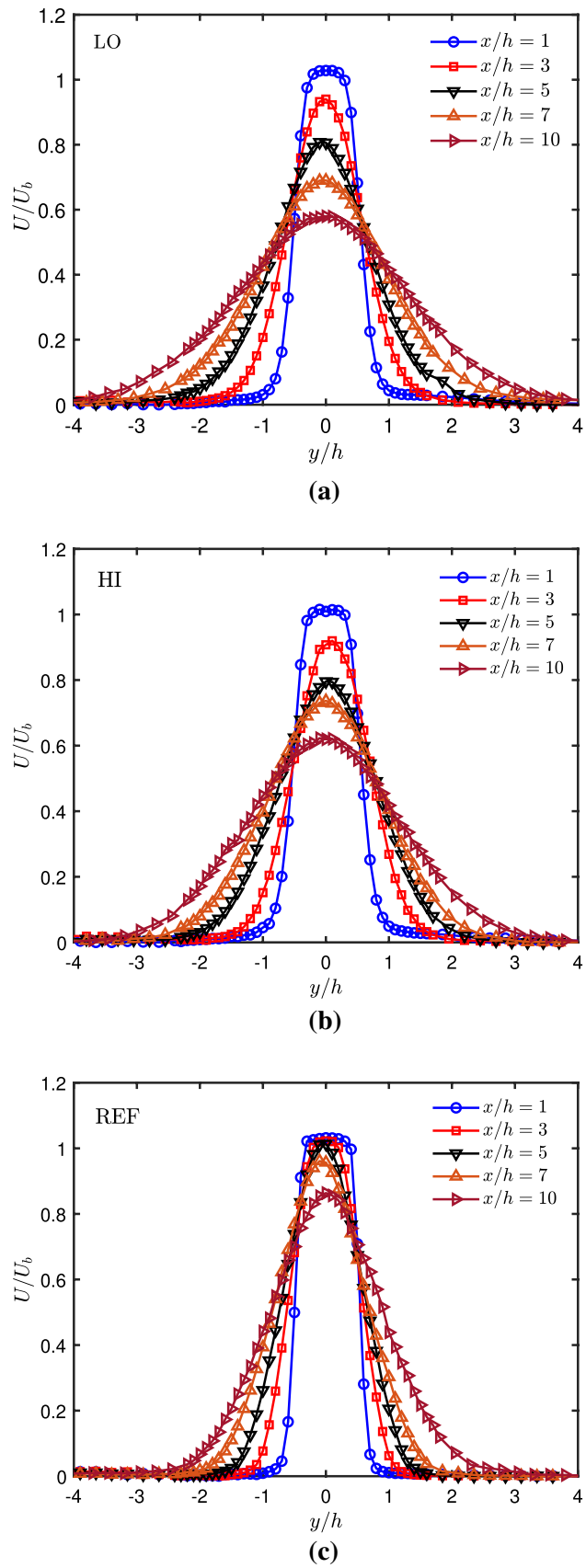

Fig. 5 Lateral mean velocity profiles for cases **a** LO, **b** HI, and **c** REF

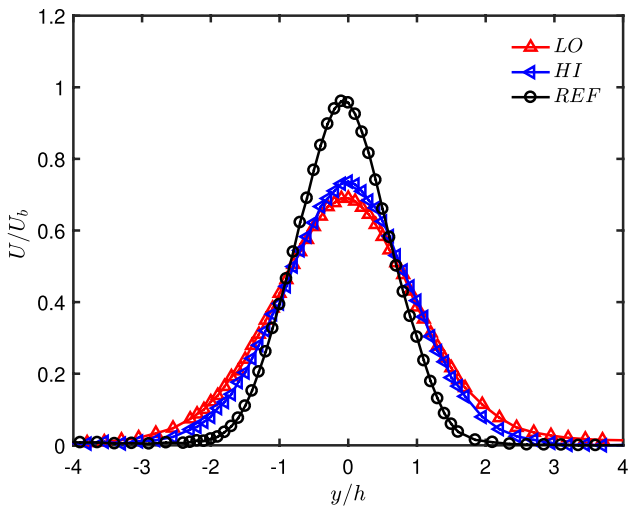

Fig. 6 Comparison of the mean velocity profiles at $x/h = 7$

scales, but significantly different turbulence intensities, we see that the increase in exit turbulence intensity results in faster jet spreading. This is likely a result of increased turbulent transport resulting from the higher turbulence intensity. Comparing LO and HI, which have similar turbulence intensities but an order of magnitude change in integral scale, we see that the smaller integral scale results in faster spreading. This is likely because the jet has evolved farther relative to its own flow length scale for LO compared to HI.

It is worth noting that both $\delta_{1/2}$ and θ are expected to grow linearly with x (Pope 2000). In particular, the wake half-width is expected to follow

$$\frac{\delta_{1/2}}{h} = K\left(\frac{x - x_0}{h}\right), \tag{1}$$

where K is the spreading rate and x_0 is a virtual origin. When looking at the far-field evolution along the jet centreline in the next section, x_0 will be useful. To find it, 'NLINFIT' in Matlab was used on Eq. 1.

The variance profiles, illustrated in Fig. 9, echo the results of the mean profiles. The active grid cases have higher turbulence intensity and wider wakes, and the REF case has lower turbulence intensity and a narrower wake. In all cases, the highest variance is observed in the shear layer. An interesting phenomenon is apparent in Fig. 10 where the cases are compared to each other for the most upstream and most downstream transverse scans. It is immediately apparent that the peak in the variance for all three cases, LO, HI and REF, is at approximately the same

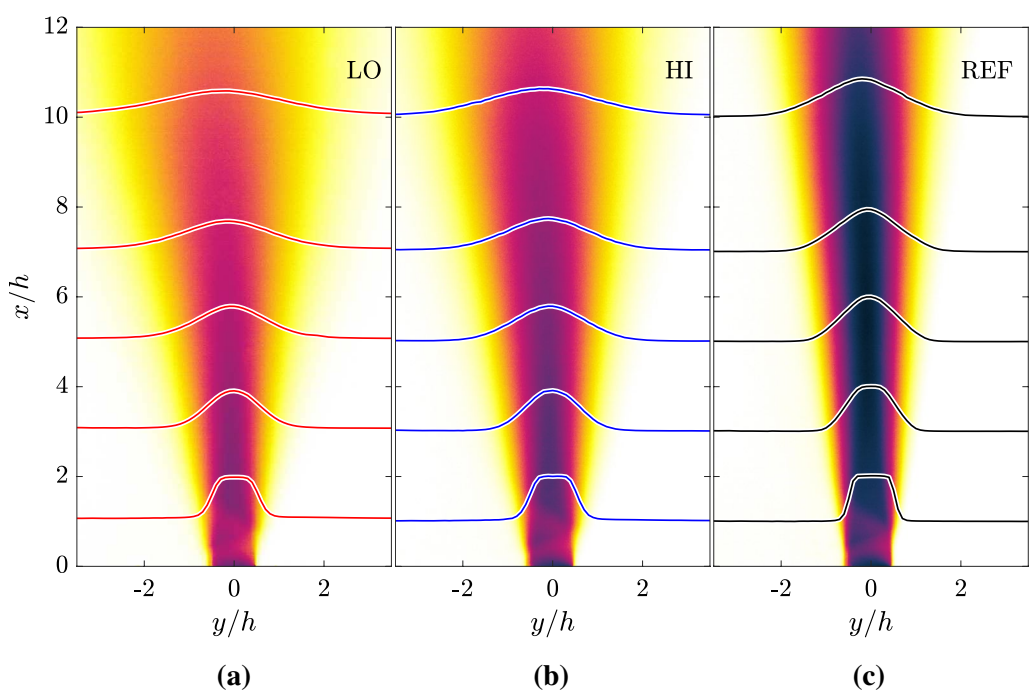

Fig. 7 Mean pixel intensity for different grid modes. The hot-wire measurements of U/U_b are superimposed at the downstream locations $x/h = 1, 3, 5, 7$ and 10. Note that $U/U_b = 0$ corresponds to the downstream position of each profile, while one unit on the x/h-axis corresponds to $U/U_b = 1$

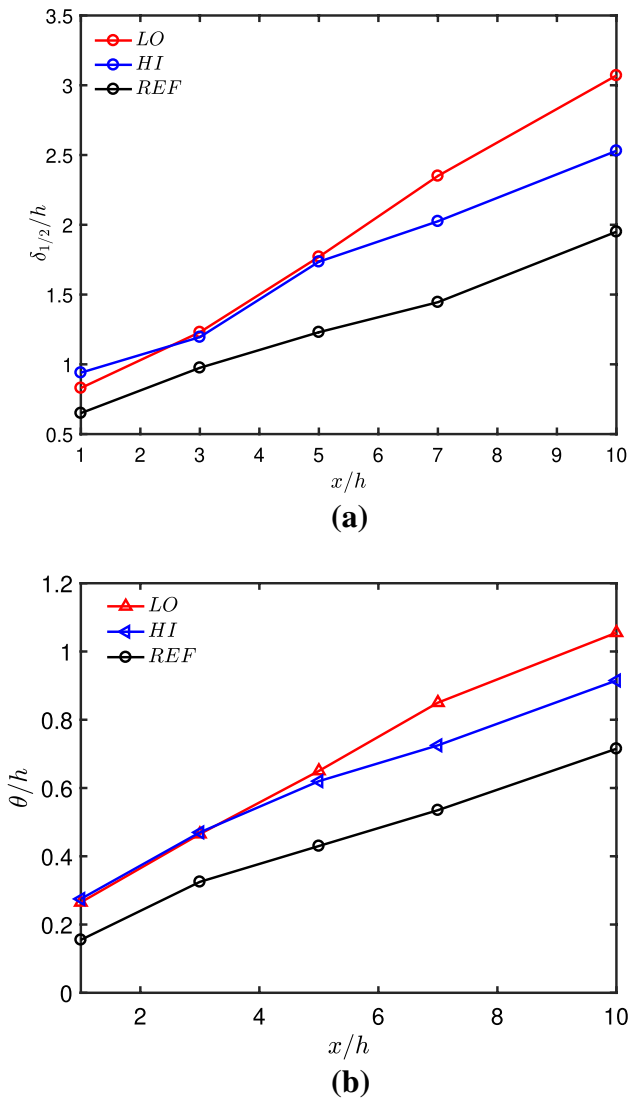

Fig. 8 Spatial evolution of the **a** wake half-width and **b** momentum thickness for the various test cases

position both at the first and final location. This suggests that while the width of the jet changes with the incoming turbulence properties, the position of maximum turbulence and mixing is relatively fixed despite the wake width itself being larger, at least in the near-field.

A first glimpse into a key difference between the two upstream turbulence cases and the REF case is visible in the variance profiles. For REF (Fig. 9c), the centreline fluctuations grow throughout the illustrated range, as expected. However, for both LO and HI, the centreline variance grows for $x/h \leq 5$, and then it starts to decrease. This suggests that the peak in the jet turbulence is not only changed in magnitude but also in physical location by adding turbulence

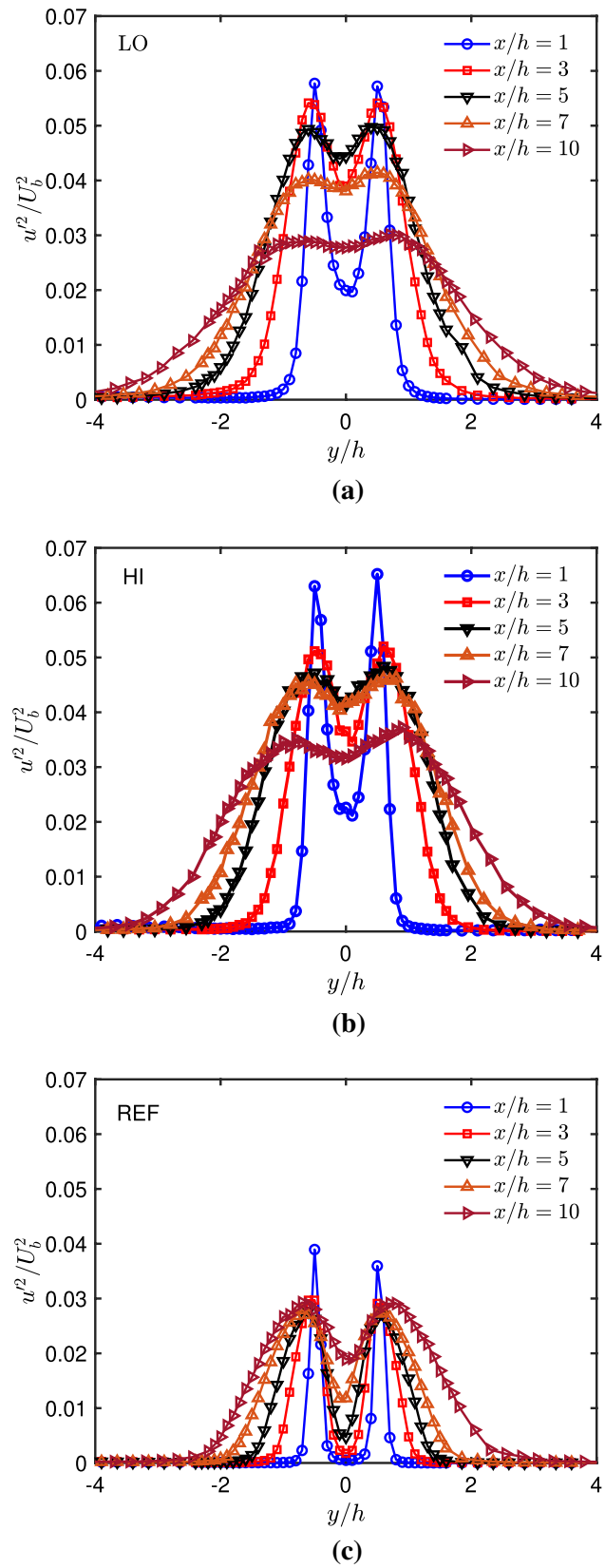

Fig. 9 Normalised variance profiles for cases **a** LO, **b** HI, and **c** REF

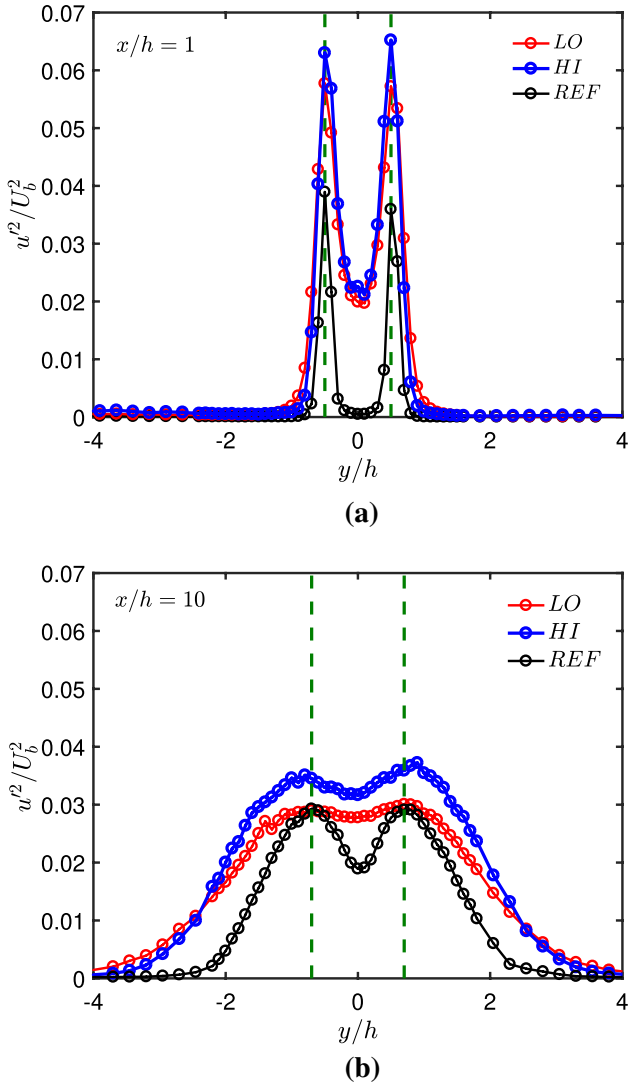

Fig. 10 Normalised variance profiles for cases LO, HI, and REF at **a** $x/h = 1$ and **b** $x/h = 10$. The vertical dashed lines represent the peak location of the variance for the REF case

upstream. For LO and HI, the peak is closer to the jet exit. This is investigated further in the next section.

While the wake width is different between LO and HI, the strength of the turbulence in the shear layers is relatively the same. This thus begs the question of what else could be different in the shear layer to result in the different wake widths. The spectra in the shear layers for all cases are plotted in Fig. 11. For the active grid cases (Fig. 11a and b), there is a peak in the spectra that corresponds to the mean rotational rate of the wings, demonstrating that the periodicity imposed on the flow upstream remains present in the shear layers.

To gain a better understanding of the structure of the shear layer, instantaneous frames from the flow visualisation focusing on the shear layer are presented in Fig. 12a. The black contour line corresponds to a constant pixel intensity. Before calculating the contour, the instantaneous frames were smoothed with a 5×5 Hanning window. The smoothing is done such that the noise at the pixel scale does not have a significant impact on the resulting contour. The selected frames are representative of the data as a whole and illustrate that the shear layer not only moves out for the LO and HI cases relative to REF, but it is also more jagged. This is quantified through the probability density function (PDF) of the position of the iso-line from all frames for each case, shown in Fig. 12b. This PDF is calculated by dividing the grid into $x/h = 0.05$ by $y/h = 0.05$ bins (corresponding to roughly the filter size). Furthermore, if an x-value corresponds to several y-values, the point with the largest y-value is used, in effect turning the iso-line into a one-to-one mapping between x and y (Kwon et al. 2014). The PDFs in Fig. 12b demonstrate that not only does the shear layer move out, but it also increases its positional variability for LO and HI compared to REF. This is further supported by Fig. 13, which is a PDF of the length of the iso-lines (L_s) identified in Fig. 12a. This quantifies that the length of the instantaneous wake boundary increases and becomes more variable for the cases (in order): REF, HI, and LO.

5 The far-field of the jet

To investigate the far-field evolution of the jet with different incoming conditions, centreline measurements were performed up to $100h$. The evolution of the centreline mean velocity is provided in Fig. 14. After the potential core region, where $U_c(x)$ remains approximately constant, it is expected to decay as $U_c(x) \sim x^{-0.5}$ (Pope 2000). For REF, such a region is approximately realised. The evolution of LO and HI is approximately collapsed, but evolves as $x^{-0.45}$. The fact that the evolution of U_c is approximately collapsed for LO and HI suggests that the centreline statistics are more dependent on the inlet turbulence intensity than the integral scale. In the far-field of all cases, the data departs from the expected trend. It is unclear at this stage if this is a result of signal-to-noise or approaching the end of our side-walls. Nonetheless, this region is not a particular focus herein.

The evolution of the streamwise velocity variance is provided for all cases in Fig. 15. The magnitude of the peak turbulence for each case scales with the incoming turbulence, as one would expect. The general relationship that

Fig. 11 One-dimensional velocity spectra in the shear layer for cases ▶ **a** LO, **b** HI, and **c** REF. For **a** and **b**, the solid vertical line represents the mean active grid wing rotational frequency, and the dashed lines represent the upper and lower bounds of the wing frequencies

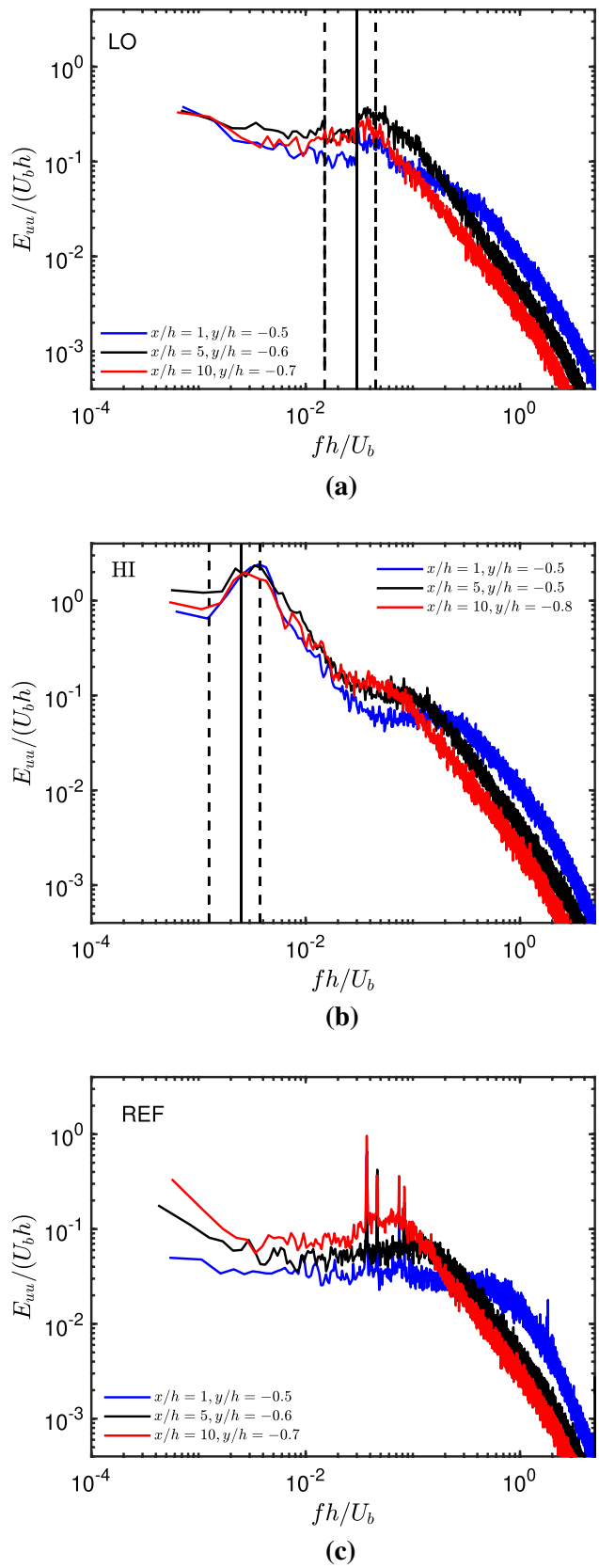

low rotational wing speeds correlate with high turbulence levels is in agreement with previous active grid turbulence research (Makita 1991; Larssen and Devenport 2011; Hearst and Lavoie 2015). Here, we explicitly confirm the observation made earlier that the peak in the variance occurs closer to the jet for increased incoming turbulence intensity. Thus, the upstream turbulence promotes the earlier development of the peak turbulence intensity and evolution of the jet flow in general.

6 Conclusion

The influence of upstream turbulence intensity and integral scale on a plane jet flow was investigated with hot-wire anemometry and flow visualisation at a fixed $\mathrm{Re}_h = 10,000$. The turbulent conditions were varied by means of an active grid placed upstream of the jet nozzle. Three cases were investigated: a canonical reference case, and two cases with elevated turbulence ($\sim 12\%$) with different integral scales.

In general, the addition of upstream turbulence resulted in faster wake spreading. If the turbulence level was kept constant, then a shorter integral scale resulted in faster spreading. Flow visualisation also revealed that the instantaneous wake width increased its variability with increased turbulence, and again a shorter integral scale increased it further.

Along the jet centreline, the addition of incoming turbulence resulted in a decrease to the decay rate of the centreline mean velocity. Furthermore, the peak in the turbulence intensity developed closer to the jet for increased turbulence. For the centreline properties, it appears the turbulence intensity plays a stronger role than the integral scale, while the integral scale dominates the outer regions of the jet.

This has been the first study of this nature generating order of magnitude changes in both the integral scale and the turbulence intesity. The information contained herein could be of great interest in numerous applications where the upstream conditions are not rigorously controlled, e.g., building ventilation. Moreover, it sheds light on disagreements between simulations and in situ measurements of such flows. In the future, a more detailed investigation of the parameter space may shed more light on how the flow behaves between the present test cases.

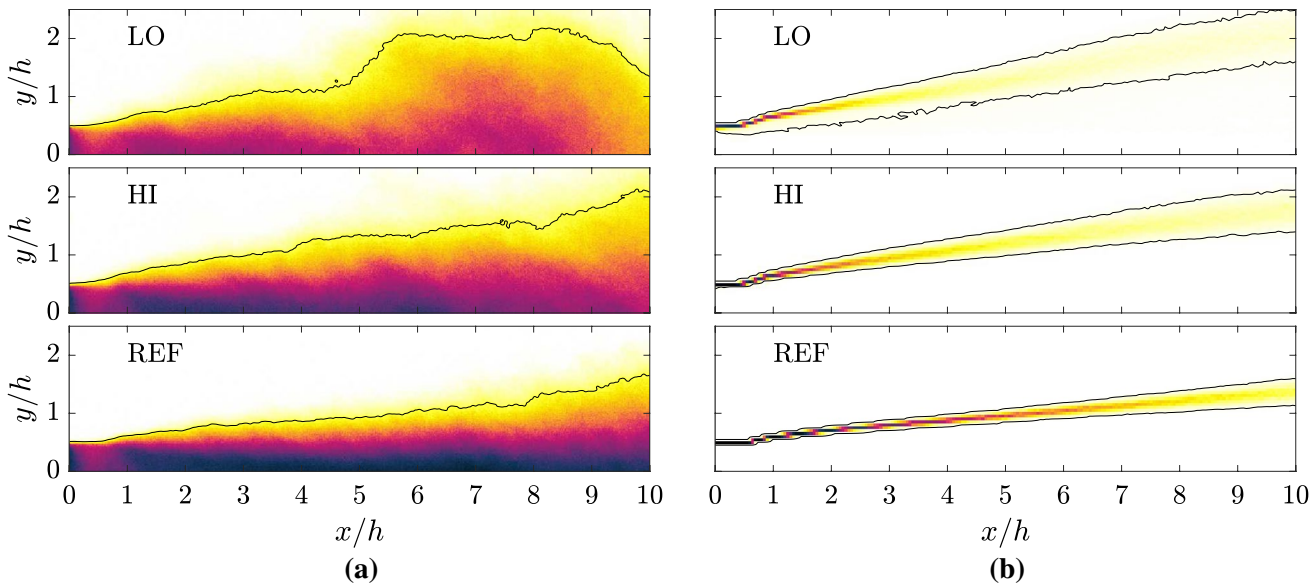

Fig. 12 **a** Instantaneous visualisations of the shear layer for the different cases. The black line represents the contour where the pixel intensity is 20% of the maximum. **b** PDF of the location of the iso-line from (**a**). The black lines represent the 0.02 probability contour

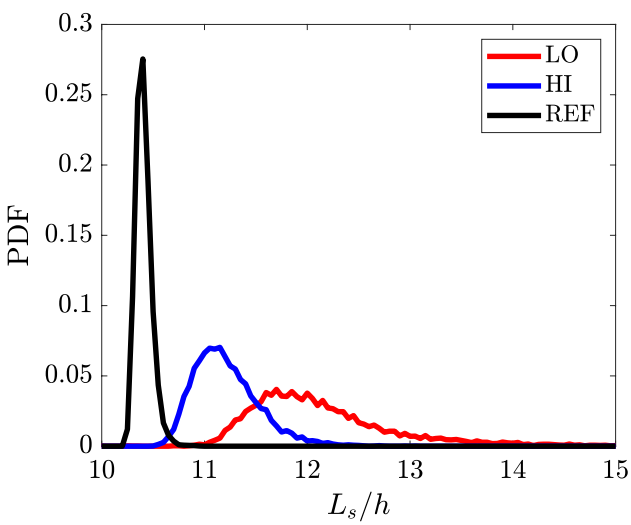

Fig. 13 PDF of the length of the iso-line from Fig. 12a. The length of the iso-line is calculated from the window $0 < x/h < 10$. Mean and peak values for the different cases are 12.14 and 11.7 for LO, 11.21 and 11.15 for HI, 10.41 and 10.4 for REF

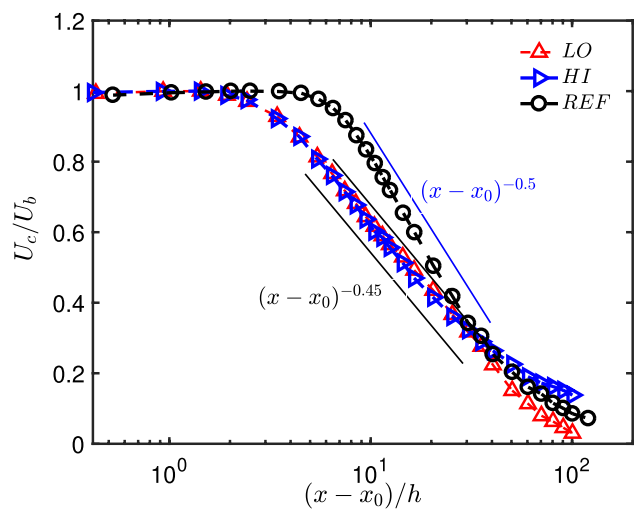

Fig. 14 Evolution of the centreline mean velocity for all cases

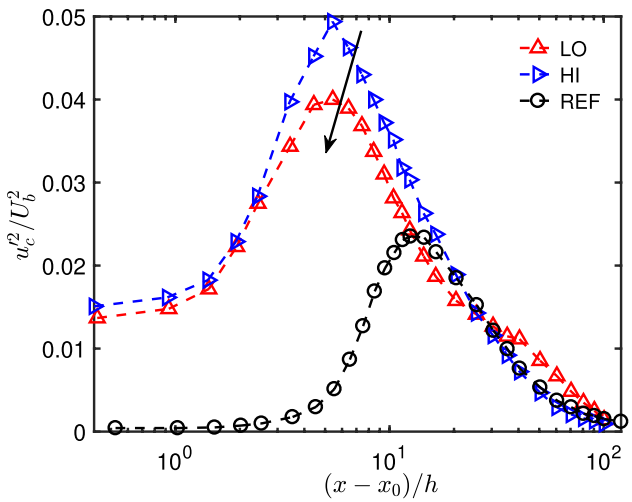

Fig. 15 Evolution of the centreline streamwise velocity variance for all cases

Acknowledgements This work was funded by the Research Council of Norway grant no. 280578 (DiHI-Tech).

Open Access This article is licensed under a Creative Commons Attribution 4.0 International License, which permits use, sharing, adaptation, distribution and reproduction in any medium or format, as long as you give appropriate credit to the original author(s) and the source, provide a link to the Creative Commons licence, and indicate if changes were made. The images or other third party material in this article are included in the article's Creative Commons licence, unless indicated otherwise in a credit line to the material. If material is not included in the article's Creative Commons licence and your intended use is not permitted by statutory regulation or exceeds the permitted use, you will need to obtain permission directly from the copyright holder. To view a copy of this licence, visit http://creativecommons.org/licenses/by/4.0/.

References

Aydemir E, Worth NA, Dawson JR (2012) The formation of vortex rings in a strongly forced round jet. Exp Fluids 52:729–742

Bashir J, Uberoi MS (1975) Experiments on turbulent structure and heat transfer in a two-dimensional jet. Phys Fluids 18(4):405–410

Cafiero G, Discetti S, Astarita T (2015) Flow field topology of submerged jets with fractal generated turbulence. Phys Fluids 27:115103

Cafiero G, Vassilicos J (2019) Non-equilibrium turbulence scalings and self-similarity in turbulent planar jets. Proc R Soc A 475(20190):038

Curvier C (2012) Active control of a separated turbulent boundary layer in adverse pressure gradient. PhD thesis 189, NNT: 2012ECLI0015:Ecole Centrale de Lille

Deo RC, Mi J, Nathan GJ (2007) The influence of nozzle aspect ratio on plane jets. Exp Therm Fluid Sci 31(8):825–838

Deo RC, Mi J, Nathan GJ (2007) The influence of nozzle-exit geometric profile on statistical properties of a turbulent plane jet. Exp Therm Fluid Sci 32(2):545–559

Deo RC, Nathan GJ, Mi J (2007) Comparison of turbulent jets issuing from rectangular nozzles with and without sidewalls. Exp Therm Fluid Sci 32(2):596–606

Deo RC, Mi J, Nathan G (2008) The influence of Reynolds number on a plane jet. Phys Fluids 20(7):075–108

George WK (1989) The self-preservation of turbulent flows and its relation to initial conditions and coherent structures. In: Arndt R, George WK (eds) Advances in turbulence. Springer, Berlin

Griffin KP, Wei NJ, Bodenschatz E, Bewley GP (2019) Control of long-range correlations in turbulence. Exp Fluids 60:55

Gutmark EJ, Grinstein FF (1999) Flow control with noncircular jets. Annu Rev Fluid Mech 31(1):239–272

Hearst RJ, Lavoie P (2014) Decay of turbulence generated by a square-fractal-element grid. J Fluid Mech 741:567–584. https://doi.org/10.1017/jfm.2013.684

Hearst RJ, Lavoie P (2015) The effect of active grid initial conditions on high Reynolds number turbulence. Exp Fluids 56(10):185. https://doi.org/10.1007/s00348-015-2052-1

Hearst RJ, Lavoie P (2016) Effects of multi-scale and regular grid geometries on decaying turbulence. J Fluid Mech 803:528–555. https://doi.org/10.1017/jfm.2016.515

Hitchman GJ, Strong AB, Slawson PR, Ray GD (1990) Turbulent plane jet with and without confining end walls. AIAA J 28(10):1699–1700. https://doi.org/10.2514/3.10460

Koochesfahani M, Dimokaris P (1989) Effects of a downstream disturbance on the structure of a turbulent plane mixing layer. AIAA J 27(2):161–166. https://doi.org/10.2514/3.10078

Krogstad PA, Davidson PA (2011) Freely decaying, homogeneous turbulence generated by multi-scale grids. J Fluid Mech 680:417–434

Krogstad PA, Davidson PA (2012) Near-field investigation of turbulence produced by multi-scale grids. Phys Fluids 24(035):103

Kumar PS, Raghavan V, Sundararajan T (2015) The effect of grids on the near-field evolution of turbulence in a low-Reynolds number jet. Phys Fluids 27:114191. https://doi.org/10.1063/1.4934822

Kwon YS, Philip J, de Silva CM, Hutchins N, Monty J (2014) The quiescent core of turbulent channel flow. J Fluid Mech 751:228–254

Larssen JV, Devenport WJ (2011) On the generation of large-scale homogeneous turbulence. Exp Fluids 50(5):1207–1223

Makita H (1991) Realization of a large-scale turbulence field in a small wind tunnel. Fluid Dyn Res 8:53–64. https://doi.org/10.1016/0169-5983(91)90030-M

Maurel S, Solliec C, Pavageau M (2000) Parametric analysis of the impinging plane air jet on a variable scaled-down mode. In: Proceedings in ASME/JSME Fluids Eng Div Summer Meeting, vol F-2277, Boston, Massachusttes

Nathan GJ, Mi J, Luxton R (2000) Centreline mixing characteristics of jets from nine differently shaped nozzles. Exp Fluids 28(1):93–94

Oster D, Wygnanski I (1982) The forced mixing layer between parallel streams. J Fluid Mech 123:91–130. https://doi.org/10.1017/S0022112082002973

Parker R, Rajagopalan S, Antonia RA (2003) Control of an axisymmetric jet using a passive ring. Exp Ther Fluid Sci 27(5):545–552

Pope SB (2000) Turbulent flows. Cambridge University Press, Cambridge. https://doi.org/10.1017/CBO9780511840531

Rajagopalan S, Antonia RA (1998) Turbulence reduction in the mixing layer of a plane jet using small cylinders. Exp Fluids 25(2):96–103

Rajagopalan S, Antonia R, Djenidi L (2013) Effect of mesh grids on the turbulent mixing layer of an axisymmetric jet. Heat Transf Eng 34(14):1216–1225

Sadeghi H, Pollard A (2012) Effects of passive control rings positioned in the shear layer and potential core of a turbulent round jet. Phys Fluids 24(115):103. https://doi.org/10.1063/1.4767535

Törnström T, Amiri S, Moshfegh B (2001) Flow and thermal characteristics of warm plane air jets (measurements and predictions using different k-ϵ models). Trans Model Simul 30:33–44

Watanabe T, Zhang X, Nagata K (2019) Direct numerical simulation of incompressible turbulent boundary layers and planar jets at high Reynolds numbers initialized with implicit large eddy simulations. Comput Fluids 194(104):314

Publisher's Note Springer Nature remains neutral with regard to jurisdictional claims in published maps and institutional affiliations.